

Forman, L.V., Bland, P.A., Timms, N.E., Daly, L., Benedix, G.K., Trimby, P.W., Collins, G.S. and Davison, T.M. (2017) Defining the mechanism for compaction of the CV chondrite parent body. *Geology*, 45(6), pp. 559-562. (doi:[10.1130/G38864.1](https://doi.org/10.1130/G38864.1))

This is the author's final accepted version.

There may be differences between this version and the published version. You are advised to consult the publisher's version if you wish to cite from it.

<http://eprints.gla.ac.uk/141177/>

Deposited on: 14 June 2017

Enlighten – Research publications by members of the University of Glasgow

<http://eprints.gla.ac.uk>

1 Defining the mechanism for compaction of the CV

2 chondrite parent body

3 **L. V. Forman^{1*}, P. A. Bland¹, N. E. Timms¹, L. Daly¹, G. K. Benedix¹, P. W.**

4 **Trimby², G. S. Collins³, and T. M. Davison³**

5 *¹Department of Applied Geology, Curtin University, GPO Box U1987, Perth, WA 6845,*
6 *Australia*

7 *²Australian Centre for Microscopy and Microanalysis, The University of Sydney, NSW,*
8 *2006, Australia*

9 *³Impact and Astromaterials Research Centre, Department of Earth Science &*
10 *Engineering, Imperial College London, Prince Consort Road, South Kensington, SW7*
11 *2BJ, UK*

12 **ABSTRACT**

13 The Allende meteorite, a relatively unaltered member of the CV carbonaceous
14 chondrite group, contains primitive crystallographic textures that can inform our
15 understanding of early Solar System planetary compaction. To test between models of
16 porosity reduction on the CV parent body, complex microstructures within ~0.5-
17 mmdiameter chondrules and ~10-μm-long matrix olivine grains were analyzed by
18 electron backscatter diffraction (EBSD) techniques. The large area map presented is one
19 of the most extensive EBSD maps to have been collected in application to extraterrestrial
20 materials. Chondrule margins preferentially exhibit limited intragrain crystallographic
21 misorientation due to localized crystal-plastic deformation. Crystallographic preferred

orientations (CPOs) preserved by matrix olivine grains are strongly coupled to grain shape, most pronounced in shortest dimension $\langle a \rangle$, yet are locally variable in orientation and strength. Lithostatic pressure within plausible chondritic model asteroids is not sufficient to drive compaction or create the observed microstructures if the aggregate was cold. Significant local variability in the orientation and intensity of compaction is also inconsistent with a global process. Detailed microstructures indicative of crystal-plastic deformation are consistent with brief heating events that were small in magnitude. When combined with a lack of sintered grains and the spatially heterogeneous CPO, ubiquitous hot isostatic pressing is unlikely to be responsible. Furthermore, Allende is the most metamorphosed CV chondrite, so if sintering occurred at all on the CV parent body it would be evident here. We conclude that the crystallographic textures observed reflect impact compaction and indicate shock-wave directionality. We therefore present some of the first significant evidence for shock compaction of the CV parent body.

INTRODUCTION

Meteorites in our collections sample both planets and small bodies within the inner Solar System. However, the process driving the lithification of these small bodies, specifically chondritic asteroids, is still debated. Meteorites preserve metamorphic textures that do not represent their state of accretion on the parent body, specifically their initial porosity (Consolmagno et al., 2008). It is therefore important to assess the microstructural evolution from high-porosity primordial materials to low-porosity meteorites.

44 Gravitational forces on chondritic asteroids have been proposed as a mechanism
45 to com- pact a highly porous body into lithified rock (Fujimura et al., 1983), as well as
46 being potentially associated with considerable planetary- scale heating (Horedt, 1980).
47 However, lithostatic pressure is low, even in objects hundreds of kilometers across
48 (Weidenschilling and Cuzzi, 2006). The weak effect of stress bridging between grains
49 would likely equilibrate over long time periods. We infer that the resultant
50 crystallographic preferred orientations (CPOs) from this process would be weak but
51 homogeneous throughout the sample, and intragrain deformation would be weak or
52 absent. If cold compaction occurred, then brittle deformation textures may arise, and
53 there would likely be a coupling of the CPO and shape preferred orientations (SPOs) of
54 the grains, owing to the lack of heat to encourage grain shape modification.

55 As an alternative model to a pure mechanical compaction, cold compaction
56 followed by radiogenic heating primarily by ^{26}Al is proposed to result in sintering of the
57 primitive grains and parent body compaction (Gail et al., 2015). This is termed hot
58 isostatic pressing (HIP), and is predicted to occur over ~ 1 m.y. (Gail et al., 2015). Olivine
59 matrix grains are predicted to be sintered at 650–700 K by surface diffusion, and
60 chondrules at >900 K by dislocation creep (Gail et al., 2015). We would therefore
61 observe consistent and homogeneous CPOs throughout the sample reflecting the
62 planetwide process and predicted time frame. If surface diffusion has modified the shape
63 of the matrix olivine grains due to growth into available pore space (Carter and Norton,
64 2013), the SPOs would likely be decoupled from the CPOs.

65 Porosity reduction in primordial chondritic asteroids may also have occurred
66 through impact-induced compaction (Bland et al., 2014; Hanna et al., 2015; Davison et

al., 2016). The shock wave produced by an impact into a porous body propagates through the medium, resulting in rapid pore collapse and localized pressure excursions over time scales of a few microseconds to seconds. Crystallographic deformation is predicted to be concentrated in initially porous regions and at the edges of chondrules, and weak, heterogeneous, and localized CPOs are likely to occur (Davison et al., 2016). Similar to cold compaction, SPOs and CPOs are expected to be coupled due to the very short time scale for heating resulting in limited modification of primary grain shapes yet alignment of grains by physical rotation.

We examined the CV3 (carbonaceous chondrite) meteorite, Allende, at microscales and mesoscales to understand the microstructural deformation and CPOs generated on the CV chondrite parent body. Allende has undergone relatively little aqueous alteration, and still contains anhydrous matrix material (although it has been at relatively higher metamorphic temperatures than other CV meteorites; Krot et al., 1998; Bonal et al., 2006). In terms of impact processing, it is classified as an unshocked S1 (Scott et al., 1992). Previous microstructural analyses of the ne-grained matrix grains of Allende ($<5\text{ }\mu\text{m}$; Scott et al., 1988) have focused on localized CPOs around individual chondrules (Watt et al., 2006; Hanna et al., 2015) and crystal- plastic deformation microstructures of selected individual chondrules, calcium-aluminum inclusions (CAIs), and matrix grains (Forman et al., 2016). Modeling of impact-induced compaction mapped the response of the chondritic medium to impact over a much larger area (256 mm^2) (Davison et al., 2016). Microscale observations from previous studies are therefore difficult to compare to modeling predictions. In this paper, crystallographic textures at mesoscales and microscales were systematically examined over a large area of 6 mm^2 ,

incorporating numerous chondrules and matrix regions. This provided a quantitative visualization of how the parent body of Allende responded to compaction, and facilitated direct comparisons with numerical simulations of different compaction processes.

METHODOLOGY

An 8 mm² area of Allende (from sample WAM 13102) was mapped to obtain phase and crystallographic data (Fig. DR1 in the GSA Data Repository¹) at a step size of 0.5 μm over 380 h, resulting in the collection of 46×10^6 electron backscattered diffraction (EBSD) patterns, representing one of the largest EBSD data sets ever collected from a single area. (Further details are provided in the Data Repository.)

A 6 mm² area of the mapped region was sub- divided into 120 ~250 × 250 μm grid squares to constrain regional and local CPOs of the fine-grained interstitial matrix olivine grains (Fig. 1). Multiple meteoritic components were included in this area, making this one of the most comprehensive EBSD applications to meteoritic materials. The right-most 2 mm² of the mapped area comprised a large, ne-grained amoeboid olivine aggregate and was therefore not included in the analysis. Large chondrule olivine grains were omitted from this analysis. Crystallographic orientations were plotted onto lower hemisphere, equal-area plots in the map x-y-z reference frame (Fig. 1) and overlain onto the phase map for spatial reference (Fig. 2). SPO fabrics of the olivine grains were quantified and the relationships between SPO and CPO were investigated (Fig. 3; Fig. DR2; see the Data Repository for methodology). All chondrule rim grains within the mapped area were also inspected for evidence of crystal- plastic deformation to characterize the deformation of chondrule margins within spatial context of the entire sample (e.g., Fig. 4), following the procedures outlined in Forman et al. (2016).

RESULTS

We identified a total of 339,040 grains; 85.3% of the grains were indexed as olivine (Fig. 2). Sparse coarse grains of clinoenstatite, spinel, and awaruite were concentrated into loose bands between chondrules, which also contained larger, rounded olivine grains (~0.02 mm). The regions immediately adjacent to chondrules (Fig. 2) primarily comprised fine-grained euhedral and subhedral olivine laths (<10 μm).

Chondrule Edge Measurements

Of the 30 chondrule grain sites, ~65% indicated as much as 5° of lattice misorientation concentrated in the outer 10–20 μm at the top or bottom of the grain (in reference frame of Fig. 2), and 25% indicated deformation that was concentrated on the right or left sides of the chondrules (e.g., Fig. 4). The remaining 10% of sites exhibited no deformation textures. Very limited lattice misorientation was detected in the chondrule interiors (<0.5°).

Grain Morphologies

Olivine matrix grains in the plane of the sample are euhedral to subhedral and lath shaped. Close inspection reveals the grains have sharp edges with minimal impingement (e.g., Fig. 3). However, small grains that are close to the step size of the EBSD mapping were omitted to avoid the geometric artifacts associated with grains defined by two pixels or less.

SPO and CPO Olivine Matrix Grain Analyses

Analyses of the SPOs and CPOs of the matrix olivines throughout the sample show that <c>, , and <a> are the long, intermediate, and short dimensions of the grains, respectively (e.g., Fig. 3). Matrix olivine grains show significant CPOs (>2.00

mean uniform density, m.u.d.) in 72 of the 120 measured regions. Of those regions, 25% had a m.u.d. of ≥ 3.00 (moderate to strong clustering of crystallographic axes). A strong point maxima CPO of $\langle a \rangle$ was observed in 68 regions (yellow arrows in Fig. 2) predominantly in the y direction (vertical) of the EBSD map (Fig. 2). The CPOs of $\langle c \rangle$ (green arrows in Fig. 2) form moderate intensity girdles that aligned with the map x direction, in 51 of the 56 regions where CPOs in $\langle c \rangle$ were observed. The CPOs of $\langle b \rangle$ (white arrows in Fig. 2) were generally weak, spatially heterogeneous point maxima with variable orientations in 14 areas directly adjacent to chondrules. These data indicate a strong coupling between grain shape (SPO) and CPO, with a predominant flattening of the matrix olivine grains parallel to the map y direction, and elongation in the map x direction (Figs. 2 and 3; Fig. DR2). The dominant CPO is observed in $\langle a \rangle$, consistent with previous studies (Watt et al., 2006).

The strongest CPOs are in close proximity to chondrule margins, with many at the top or bottom of chondrules, or in between closely spaced (< 0.1 mm) chondrules (Fig. 2). Strong, localized variations of the overall CPOs are evident around chondrules (Fig. 2), where grains are attenuated against the chondrule margins.

DISCUSSION

Matrix olivine grains in Allende have preserved euhedral-subhedral lath morphologies. They have a moderate SPO throughout the mapped region, which correlates consistently to the observed CPO, indicating that a flattening fabric of variable strength has been produced. The relationship between CPO and SPO implies that sintering and surface diffusion have not occurred, therefore the CV parent body was not at the high temperatures required for HIP to occur over the required time scales. If

159 subgrain rotation recrystallization had generated the CPOs, rotation through large angles
160 would be required, which would act to reduce the aspect ratio of the matrix laths. Because
161 the matrix laths are elongate, some primary porosity is still present, and crystalplastic
162 deformation effects are minor (Forman et al., 2016), the CPO is predominantly the result
163 of the physical realignment of anisotropic olivine grains rather than dislocation or
164 diffusion creep.

165 The minor crystal-plastic strain observed at the margins of chondrules and a lack
166 of such strain in chondrule interiors indicate Allende must have undergone high (but
167 transient) stresses and temperatures during deformation (Frost and
168 Ashby, 1982), at a local scale. Comparatively, matrix olivine grains have
169 undergone significantly more intragrain deformation (Forman et al., 2016), which is
170 inferred to result from brief localized temperature excursions predicted from
171 impactinduced compaction. Allende is expected to have been at temperatures between
172 300 and 800 K (e.g., Weinbruch et al., 1994; Huss et al., 2006; Cody et al., 2008),
173 implying that sintering within Allende could only have been achieved in matrix grains,
174 and any temperature excursion above that threshold was not sustained for a significantly
175 long period of time, and certainly not for durations on the order of 1 m.y.

176 Local variations in CPO alignment and intensity were observed over a small area of
177 6 mm² at the mesoscale, and are consistent with previous EBSD studies (Watt et al.,
178 2006). It has been argued that stress applied by lithostatic forces within the parent
179 asteroid were negligible (1 MPa at the center of a 200-km-diameter body;
180 Weidenschilling and Cuzzi, 2006). In addition, uniform, planetary-scale compaction of a
181 highly porous, low-gravity small planetary body would not generate such localized

182 textures because stress bridging between grains would have equilibrated over time, nor
183 would it have created discrepancies in deformation between chondritic components.
184 Heating to $>500\text{ }^{\circ}\text{C}$ and compaction associated with HIP or hot gravitational compression
185 would have been sustained over a time period of $\sim 1\text{ m.y.}$ (Gail et al., 2015). Rheological
186 constraints from olivine (Karato et al., 1986) indicate that significant diffusion creep is
187 predicted, at this temperature, time frame, and matrix grain size, that would have reduced
188 porosity in a homogeneous way via diffusion creep recrystallization and new grain
189 growth, and resulted in a recovered and annealed microstructure. However, as this was
190 not observed HIP is unlikely to have contributed to the textural development of Allende.
191 Because Allende is the most thermally altered CV chondrite studied (Bonal et al., 2006;
192 Cody et al., 2008) this argument applies to the entire suite of CV chondrites.

193 Impact-induced compaction would generate shock-wave interactions with chondritic
194 components, and associated localized heating and compression throughout the parent
195 body over short time scales that would be rapidly equilibrated following the compression
196 event (Davison et al., 2012; Bland et al., 2014). The collapse of abundant pores adjacent
197 to chondrule edges is predicted to generate localized temperature excursions (to $\sim 850\text{ K}$
198 in a 1.5 km/s impact into a mixture of 70% porous matrix and non- porous chondrules,
199 with a bulk porosity of 50%; Bland et al., 2014) when compared to nonporous regions,
200 i.e., chondrule interiors ($\sim 330\text{ K}$ in the same scenario; Bland et al., 2014). This brief
201 heating discrepancy easily explains the deformational textures in chondrule and matrix
202 grains, and would be associated with heterogeneous SPOs and CPOs that are also likely
203 to be asymmetric around chondrules. As heat production is the result of pore collapse due

to compression, regions that experienced the highest temperatures are the same regions that underwent the most compression, and therefore formed the most significant CPOs.

CONCLUSIONS

We examined the crystallographic textural features at both the microscales and mesoscales within the CV3 chondrite Allende using one of the most comprehensive EBSD maps ever collected, to explore compaction processes on the CV chondrite parent body. Abundant but minimal chondrule edge lattice deformations that are not uniformly distributed around chondrule margins and moderately strong yet heterogeneously oriented $\langle a \rangle$ axis CPOs and coupled SPOs were detected throughout the ne-grained matrix regions, consistent with a variably developed flattening fabric. Allende has also been at higher temperatures than other CVs. If sintering, and therefore HIP, had occurred we would see microstructural evidence of it in this sample. Our observations rule out HIP and other forms of gravity-driven compaction as viable compaction processes of the CV parent body, and by inference any small primitive bodies. Impact-induced compaction provides the required heterogeneous distribution of heating and compaction over a short time scale, and our findings closely replicate the small-scale spatial heterogeneities predicted by numerical modeling. The orientations of the SPOs and CPOs in association with chondrule edge lattice deformations provide directionality for shock-wave propagation; compaction was parallel to the y direction of Figure 2 and occurred primarily due to impacts into the highly porous parent body.

This unique study is one of the first to identify crystallographic evidence for impact-induced compaction of the CV parent body, and therefore is a very significant

application of EBSD techniques to meteorites. Although this finding is limited to formation of the CV parent body in this study, small planetary bodies would likely have undergone similar impacts, and would have small lithostatic pressures acting to compact the body. There is therefore scope to expand this approach to other chondrites and small parent bodies.

ACKNOWLEDGMENTS

This work was funded by the Australian Research Council via the Australian Laureate Fellowship program (FL110100074 to Bland). We acknowledge the technical assistance and use of facilities at the University of Sydney node of the Australian Microscopy and Microanalysis Research Facility. Collins and Davison were funded by UK Science and Technology Facilities Council grant ST/N000803/1. We thank editor Bob Holdsworth, reviewer Jon Friedrich, and two anonymous reviewers for constructive comments.

REFERENCES CITED

- Bland, P.A., Collins, G.S., Davison, T.M., Abreu, N.M., Ciesla, F.J., Muxworthy, A.R., and Moore, J., 2014, Pressure-temperature evolution of primordial solar system solids during impact-induced compaction: *Nature Communications*, v. 5, 5451, doi:10.1038/ncomms6451.
- Bonal, L., Quirico, E., Bourot-Denise, M., and Montagnac, G., 2006, Determination of the petrologic type of CV3 chondrites by Raman spectroscopy of included organic matter: *Geochimica et Cosmochimica Acta*, v. 70, p. 1849–1863, doi:10.1016/j.gca.2005.12.004.

247 Carter, C.B., and Norton, M.G., 2013, Sintering and grain growth, *in* Carter, C.B., and
 248 Norton, G.M., *Ceramic materials: Science and engineering*: Springer, New York, p.
 249 439–456, doi:10.1007 /978-1-4614-3523-5_24.
 250 Cody, G.D., Alexander, C.O.D., Yabuta, H., Kilcoyne, A.L.D., Araki, T., Ade, H., Dera,
 251 P., Fogel, M., Militzer, B., and Mysen, B.O., 2008, Organic thermometry for
 252 chondritic parent bodies: *Earth and Planetary Science Letters*, v. 272, p. 446–455,
 253 doi:10.1016/j.epsl.2008.05.008.
 254 Consolmagno, G.J., Britt, D.T., and Macke, R.J., 2008, The significance of meteorite
 255 density and porosity: *Chemie der Erde*, v. 68, p. 1–29,
 256 doi:10.1016/j.chemer.2008.01.003.
 257 Davison, T.M., Ciesla, F.J., and Collins, G.S., 2012, Post-impact thermal evolution of
 258 porous planetesimals: *Geochimica et Cosmochimica Acta*, v. 95, p. 252–269,
 259 doi:10.1016/j.gca.2012.08.001.
 260 Davison, T.M., Collins, G.S., and Bland, P.A., 2016, Mesoscale modeling of impact
 261 compaction of primitive solar system solids: *Astrophysical Journal*, v. 821, p. 68.
 262 Forman, L.V., et al., 2016, Hidden secrets of deformation: Impact-induced compaction
 263 within a CV chondrite: *Earth and Planetary Science Letters*, v. 452, p. 133–145,
 264 doi:10.1016/j.epsl.2016.07.050.
 265 Frost, H.J., and Ashby, M.F., 1982, *Deformation-mechanism maps: The plasticity and*
 266 *creep of metals and ceramics*: Oxford, UK, Pergamon Press, 165 p.
 267 Fujimura, A., Kato, M., and Kamazawa, M., 1983, Preferred orientation of phyllosilicate
 268 (001) in matrix of Murchison meteorite and possible mechanisms of generating the

269 oriented texture in chondrites: *Earth and Planetary Science Letters*, v. 66, p. 25– 32,
 270 doi:10.1016/0012-821X(83)90123-1.

271 Gail, H.P., Henke, S., and Tieloff, M., 2015, Thermal evolution and sintering of
 272 chondritic planetesimals—II. Improved treatment of the compaction process:
 273 *Astronomy & Astrophysics*, v. 576, A60, doi:10.1051/0004-6361/201424278.
 274 Hanna, R.D., Ketcham, R.A., Zolensky, M., and Behr, W., 2015, Impact-induced brittle
 275 deformation, porosity loss, and aqueous alteration in the Murchison CM chondrite:
 276 *Geochimica et Cosmochimica Acta*, v. 171, p. 256–282,
 277 doi:10.1016/j.gca.2015.09.005.

278 Horedt, G.P., 1980, Gravitational heating of planets: *Physics of the Earth and Planetary*
 279 *Interiors*, v. 21, p. 22–30, doi:10.1016/0031-9201(80)90016-3.

280 Huss, G.R., Rubin, A.E., and Grossman, J.N., 2006, Thermal metamorphism in
 281 chondrites, *in* Lauretta, D.S., and McSween, H.Y., eds., *Meteorites and the early*
 282 *Solar System II*: Tuscan, University of Arizona Press, p. 567–586.

283 Karato, S.I., Paterson, M.S., and FitzGerald, J.D., 1986, Rheology of synthetic olivine
 284 aggregates: Influence of grain size and water: *Journal of Geophysical Research*, v.
 285 91, p. 8151–8176, doi:10.1029/JB091iB08p08151.

286 Krot, A.N., Petaev, M.I., Scott, E.R., Choi, B.G., Zolensky, M.E., and Keil, K., 1998,
 287 Progressive alteration in CV3 chondrites: More evidence for asteroidal alteration:
 288 *Meteoritics & Planetary Science*, v. 33, p. 1065–1085,
 289 doi:10.1111/j.19455100.1998.tb01713.x.

290 Scott, E.R.D., Barber, D.J., Alexander, C.M., Hutchison, R., and Peck, J.A., 1988,
 291 Primitive material surviving in chondrites: Matrix, *in* Kerridge, J.F., and Matthews,

292 M.S., eds., *Meteorites and the early Solar System*: Tucson, University of Arizona
 293 Press, p. 718–745.

294 Scott, E.R.D., Keil, K., and Stöffler, D., 1992, Shock metamorphism of carbonaceous
 295 chondrites: *Geochimica et Cosmochimica Acta*, v. 56, p. 4281– 4293,
 296 doi:10.1016/0016-7037(92)90268-N.

297 Watt, L.E., Bland, P.A., Prior, D.J., and Russell, S.S., 2006, Fabric analysis of Allende
 298 matrix using EBSD: *Meteoritics & Planetary Science*, v. 41, p. 989–1001,
 299 doi:10.1111/j.1945-5100.2006.tb00499.x.

300 Weidenschilling, S.J., and Cuzzi, J.N., 2006, Accretion dynamics and timescales:
 301 Relation to chondrites, *in* Lauretta, D.S., and McSween, H.Y., eds., *Meteorites and*
 302 *the early Solar System II*: Tuscon, University of Arizona Press, p. 473–485.

303 Weinbruch, S., Armstrong, J., and Palme, H., 1994, Constraints on the thermal history of
 304 the Allende parent body as derived from olivine-spinel thermometry and Fe/Mg
 305 interdiffusion in olivine: *Geochimica et Cosmochimica Acta*, v. 58, p. 1019– 1030,
 306 doi:10.1016/0016-7037(94)90523-1.

307

308 Manuscript received 5 December 2016

309 Revised manuscript received 15 February 2017

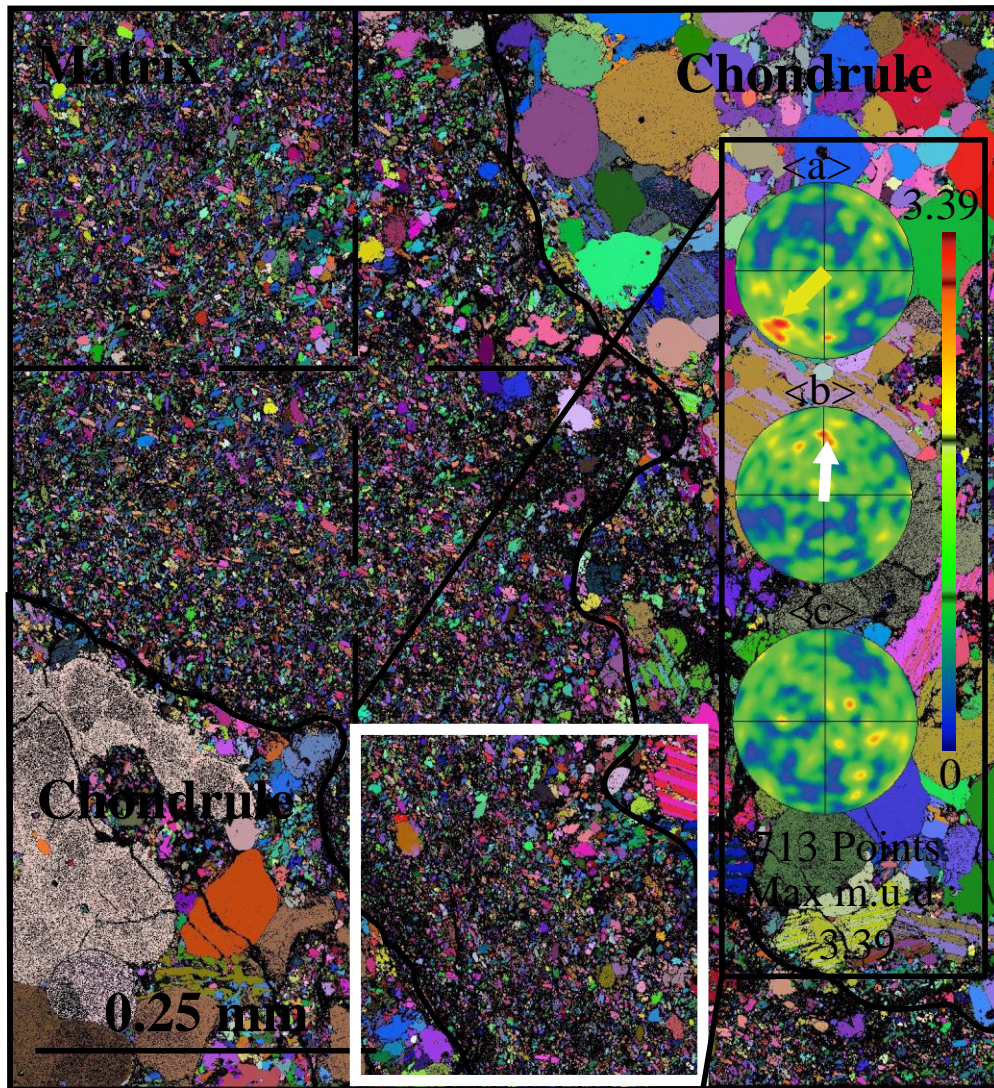
310 Manuscript accepted 7 March 2017

311 Printed in USA

312

313 FIGURES

Figure 1. The mapped area of Allende was divided into a grid (euler map is background). The orientations of the crystallographic axes for each matrix grain were plotted onto lower hemisphere, equal area plots to identify CPOs. In this case, a moderate $\langle a \rangle$ axis CPO perpendicular to the chondrule edge and weak $\langle b \rangle$ axis CPO parallel to the chondrule edge are observed.



321 Figure 2. Full CPO analysis overlaid onto the phase map. Black regions are chondrules.
322 Colored arrows within gray circles indicate an alignment of the crystallographic axes.
323 The thickness of each line reflects the m.u.d. of the CPO. Double ended arrows indicate
324 the axis cluster lies on the edge of the lower hemi plot, indicating this axis is parallel to
325 the plane of the sample (i.e., x-y reference plane shown here). The dominant CPO is in
326 $\langle a \rangle$ (yellow lines) which lies predominantly parallel to the y-axis of the reference plane,
327 but also shows localized deviations at chondrule edges.

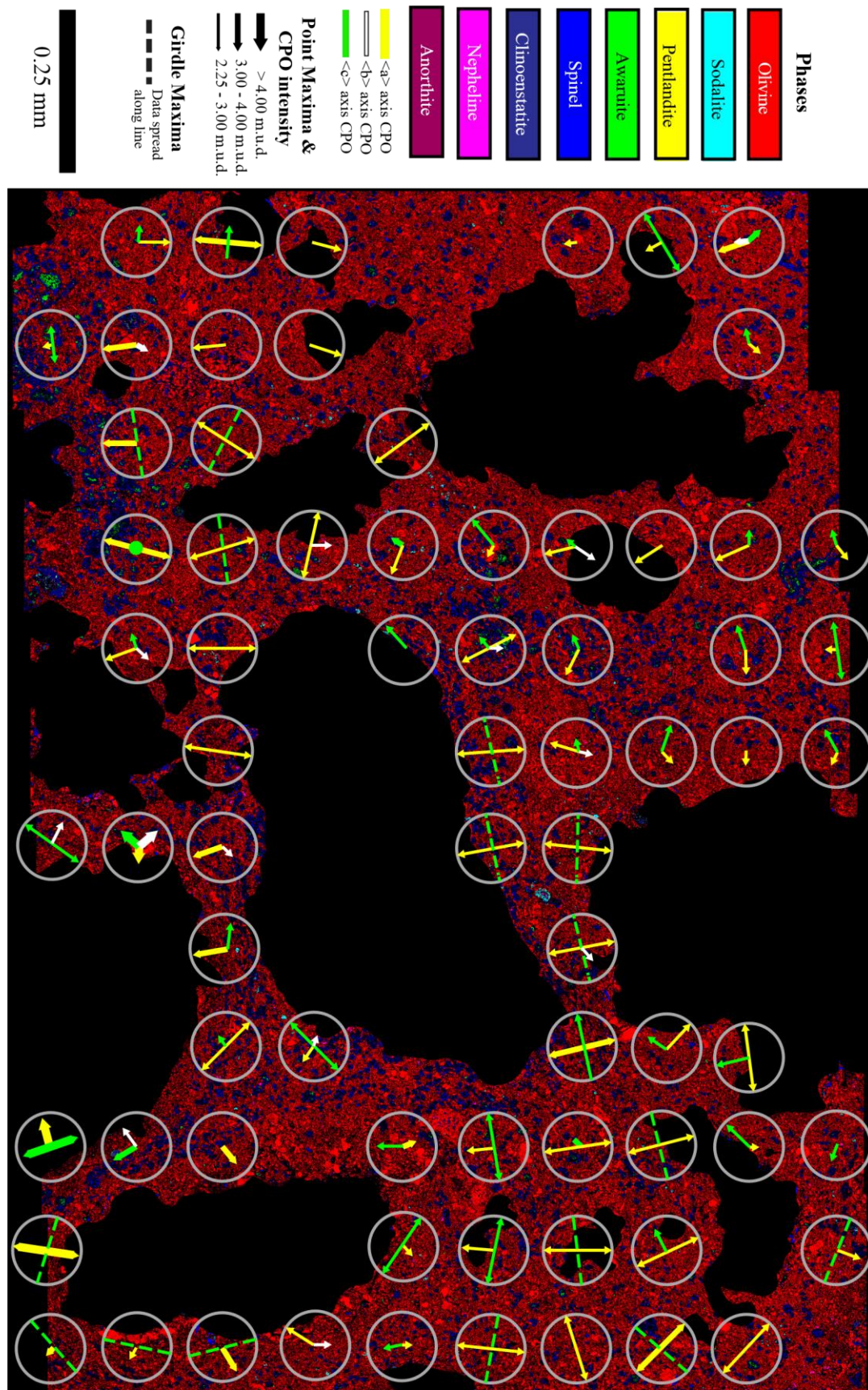


Figure 3. Shape analysis of matrix olivine grains demonstrated on a small region of the total area. a) map color coded to indicate orientation of long axis of the fitted ellipse (fitted ellipses= black ovals) for each matrix olivine, b) Pole figures of subset (iii) of the total matrix olivine data set. Top shows $\langle a \rangle$, $\langle b \rangle$ and $\langle c \rangle$ with one point per grain in map color scheme, and below is the contoured data. These indicate the CPO and SPO of this region are coupled; the crystallographic orientation of each grain is strongly correlated to the grain shape. Lower hemisphere equal area plots in map x-y-z reference frame.

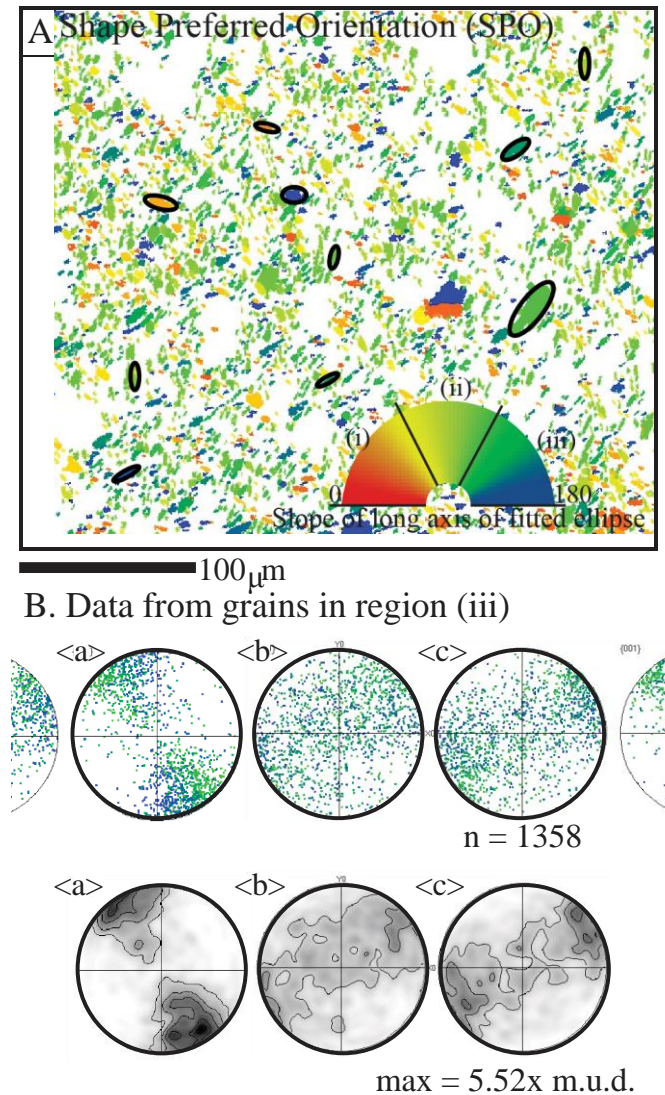
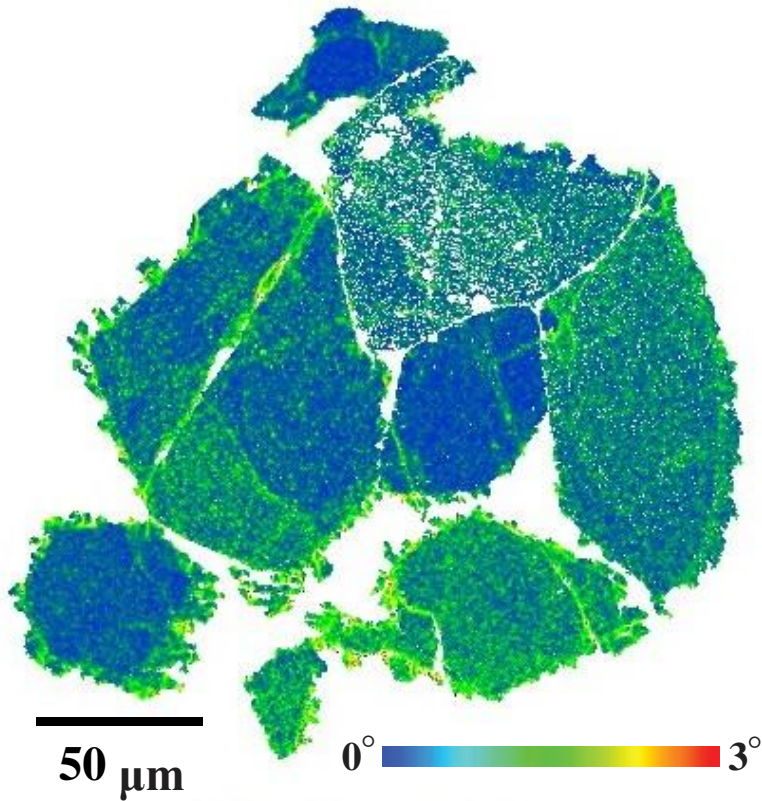


Figure 4. Chondrule olivine grains showing crystallographic deformation concentrated toward the bottom of the chondrule. Local misorientation map is color coded to

340 demonstrate the deviation of crystallographic orientation of each pixel with relation to the
341 orientation of the surrounding 8 pixels (measured in degrees/1.5 μm).



342

343

344 ¹GSA Data Repository item 2017xxx, xxxxxxxx, is available online at

345 www.geosociety.org/datarepository/2017 or on request from editing@geosociety.org.

346 Data repository files:

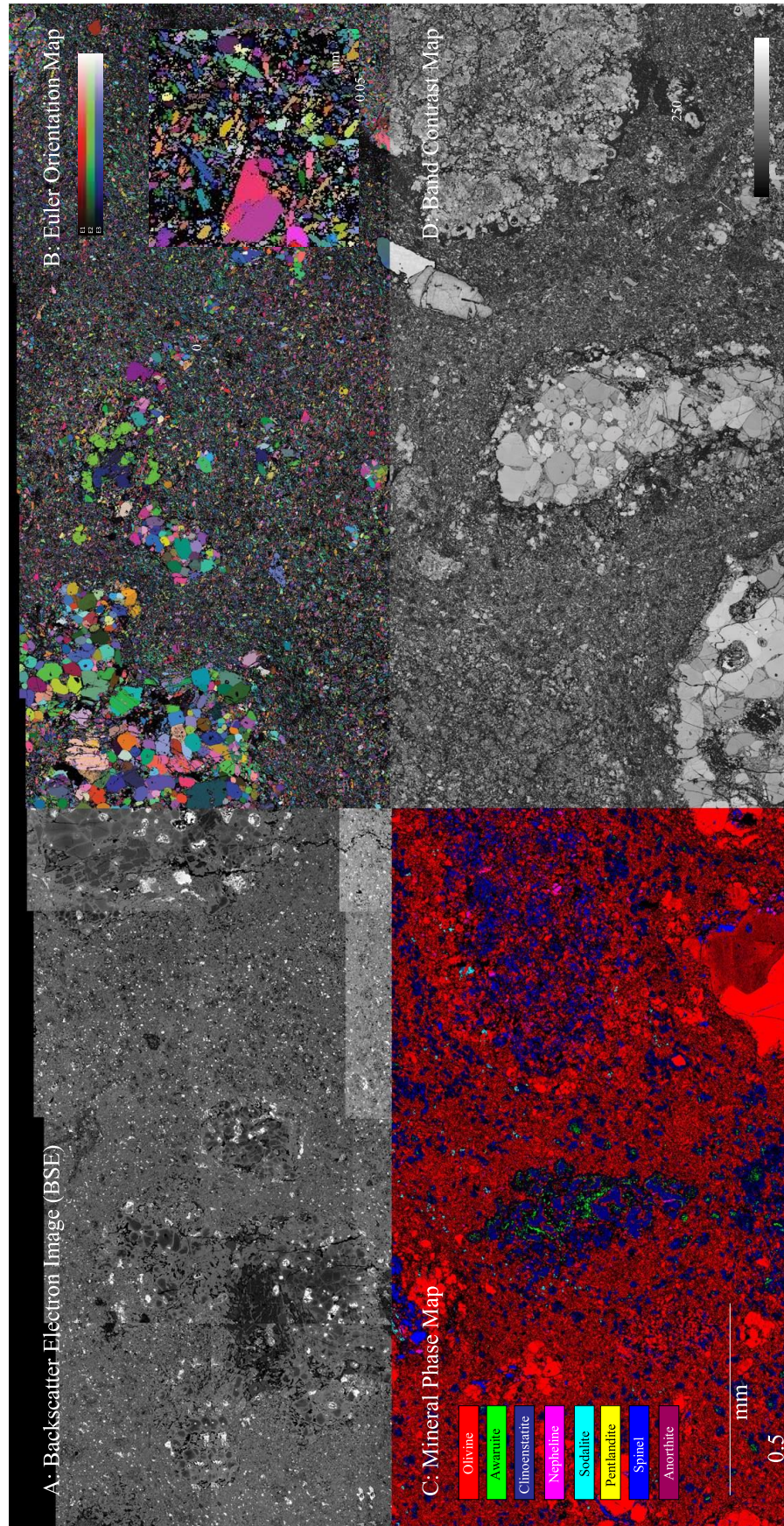


Figure 1: Map of Allende shown with four different imaging techniques- a) backscatter electron image (BSE), b) all euler orientation map, colour coded to reflect collective crystallographic orientation with respect to the three primary crystallographic axes of each grain, c) mineral phase map, where bright regions indicate a strong diffraction pattern and dark regions indicate a weak or absent diffraction pattern.

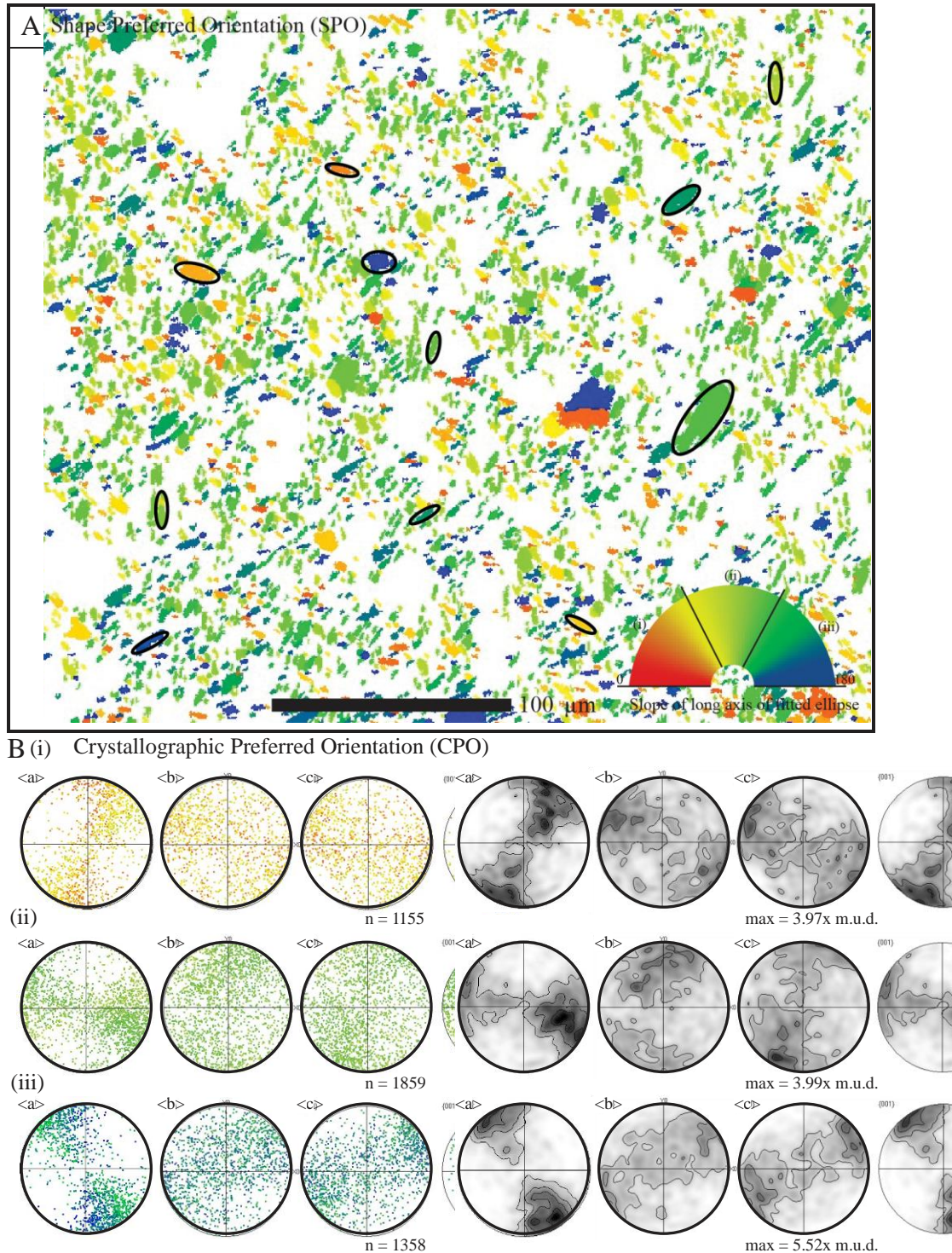


Figure 2: Shape analysis of matrix olivines- a) map colour coded to indicate orientation of long axis of the fitted ellipse for each matrix olivine, b) grains divided into subsets i, ii and iii. Lower hemisphere, equal area plots show one point per grain for each grain in the subset on the left, and the contoured data is displayed on the right.

Data Repository- Methodology

Detailed Methodology

An 8 mm² area of Allende was mapped using a Carl Zeiss Ultra Plus field emission gun scanning electron microscope (FEG SEM) at the University of Sydney node of the Australian Microscopy & Microanalysis Research Facility. Element, phase and crystallographic data maps (Supplementary material fig. 1) were collected at a step size of 0.5 µm over 380 hours, using both the NordlysNano EBSD detector and X-Max 20 silicon drift detector (EDS), using 20 keV accelerating voltage and 10 nA current. This resulted in the detection of over 46 million diffraction patterns, and 7 billion x-rays. The EBSD patterns were indexing using Oxford Instruments AZtec software, and resulting orientation maps were processed using the Oxford Instruments CHANNEL 5.12 system. Data were noise reduced as per the procedure outlined by Watt et al. (2006), and grains smaller than 1.5 µm (3 x step size of 0.5µm) were disregarded for further analysis to conservatively account for any potential mapping artefacts.

30 chondrules or chondrule rim grains within the mapped area were inspected for evidence of crystal-plastic deformation to constrain chondrule edge deformation within spatial context. For a detailed description of the chondrule deformation measurement, we direct the reader to the procedures of Forman et al., (2016).

CPO analysis required a subdivision of the mapped region into 120 grid squares to identify local and regional textures between olivine matrix grains (Fig. 1). The collective crystallographic orientations within each grid square were plotted onto lower hemisphere, equal area plots (Fig. 1) and overlain on the phase map for spatial reference (Figs. 1 & 2).

One point per grain was plotted to avoid data bias. Both point and girdle maximas were observed. Point maximas are indicated by an arrow from the centre of the plot to the axes clusters (e.g. in fig. 1), and double-ended arrows are used where the point maxima are positioned on the edge of the plot. A dotted line is used for girdle maximas. The thickness of each line specifies the intensity of the CPO present (mean uniform density (m.u.d.)). This approach allowed for an effective visual representation of the three primary crystallographic axes from ~2000 grains in one plot within their spatial context, and allowed for cross-examination of localised and overall CPOs from a broad area. To comprehend our CPO data, a comparison with shape-preferred orientation of the olivine grains was necessary (Fig. 3). The full analytical process is detailed in figure 3 and supplementary material figure 2.